DOI: 10.13009/EUCASS2023-282
Aerospace Europe Conference 2023 – 10TH EUCASS – 9TH CEAS

Effects of magnetic nozzle strength on a supersonic ion beam in a RF electrode-less plasma thruster

Antonella Caldarelli[1†], *Félicien Filleul*[1], *Christine Charles*[2], *Roderick Boswell*[2], *John Cater*[3] *and Nicholas Rattenbury*[1]
[1]*Department of Physics, The University of Auckland*
[2]*Research School of Physics, The Australian National University*
[3]*Department of Mechanical Engineering, University of Canterbury*
[†]Corresponding author
antonella.caldarelli@auckland.ac.nz
38 Princes Street, Auckland, New Zealand

Abstract

For propulsive applications, it is important to understand the expansion of a supersonic ion beam in a magnetic nozzle as it is one of the main thrust generation mechanisms in electrode-less radio-frequency plasma thrusters. The present study discusses the effects of magnetic field strength on the axial characteristics of an ion beam. Experiments are conducted in a radio-frequency magnetic nozzle plasma device at The University of Auckland with four different magnetic field strengths configurations. A four-grid retarding field energy analyser is used to measure the local plasma and ion beam potentials, the axial evolution of the ion energy distribution functions, and to estimate the ion beam density and speed. While greater ion beam speeds are measured at the lower magnetic field strengths ($\sim$ 10 km/s compared to $\sim$ 9 km/s for the highest field case), the ion beam current collected at the maximum magnetic nozzle strength is found to be nine times higher than that for the minimum field case. This behaviour is evidenced by the rise in amplitude of the ion beam energy distribution measured for higher magnetic field strengths. The axial transport of the ion beam is also observed to be modified by the magnetic nozzle strength. As the magnitude of $\vec{B}$ increases, the presence of an ion beam is detected over longer axial distances.

1. Introduction

Radio-frequency (RF) electrode-less plasma thrusters are a type of electric propulsion (EP) system that employs radio-frequency excitation to generate the plasma and a magnetic nozzle (MN) to enhance plasma acceleration and confinement, and to convert the electron internal energy into the directed kinetic energy of the ions.[1,2] This new technology has received a lot of interest in the EP community in the last two decades, as its numerous benefits could make it a competitive choice for future low-thrust space missions. When compared to gridded ion engines and Hall Effect thrusters, the lack of electrodes and neutralisers of the RF plasma thruster's design, together with the advantage of a magnetic nozzle in improving plasma confinement, could increase the lifetime of the propulsion system. Additionally, the concept of magnetic thrust vectoring (MTV) for radio-frequency plasma thrusters, which relies on a steerable magnetic nozzle to control the direction of the plasma plume, has been proposed.[3–8] The capability to tune the magnetic field configuration would enable full modulation of the in-flight thrust profile of the spacecraft. However, the highest efficiency reached so far during the testing campaigns has been 30%.[9]

In order to make MN plasma thrusters a competitive choice with respect to current employed electric propulsion systems, the coupling of the expanding plasma with the magnetic nozzle has to be fully understood. Since the thrust is directly associated with the axial momentum flux exhausted from the system,[10] the ion beam speed and density are important parameters to maximise in order to improve the efficiency of RF electrode-less plasma thrusters. The scope of this study is to present measurements of an RF plasma expanding in a magnetic nozzle under different magnetic field configurations. As the focus is on future thruster applications, the work is aimed at the characterisation of an accelerated ion beam. A controllable 3D magnetic nozzle, whose designed was based on the study carried out by Merino et al. (2017),[4] was incorporated and tested into *Moa*, a new RF plasma device apparatus dedicated to the research of magnetic nozzle radio-frequency plasma thrusters at the University of Auckland. Spatially resolved measurements of the plasma characteristics during the expansion phase are presented to study how changing magnetic field strength affects the ion acceleration. The ambipolar electric field on axis, the beam density and speed, and the ion energy distribution functions are investigated from measurements obtained with an emissive probe and a retarding field energy analyser.

DOI: 10.13009/EUCASS2023-282

2. Experimental set-up

The experiments presented are conducted in *Moa*, a radio-frequency plasma device designed and built at The University of Auckland. The set-up, shown in figure 1, comprises a 45 mm-radius 0.5 mm-thick borosilicate glass plasma source connected to a 250 mm-radius stainless steel expansion chamber. The axial location of the interface between the source and the chamber is defined as the centre of *Moa*'s coordinate system, i.e. $(r, z) = (0, 0)$ cm. The plasma is excited by a 1.3 loop antenna through a 1 kW power supply and at a 27.12 MHz driving frequency. The reflected power during the experiments is always kept below 1% via an L-type matching network mounted between the RF power supply and the antenna. The system is maintained at high vacuum through a turbo-molecular pump with an approximately 700 L/s pumping capability. A base pressure of $\sim 10^{-7}$ Torr is routinely achieved, and it is monitored by a full range Pirani inverted magnetron gauge. The symmetric convergent-divergent magnetic field is created by a set of three, concentric solenoids mounted as close as possible to the plasma source/expansion chamber interface. While the antenna is commonly placed at the same axial location of the coils, in this apparatus the antenna is located further away ($z_{\mathrm{Ant}} = -18$ cm and $z_{\mathrm{Coil}} = -8$ c); thus, the location of plasma excitation is decoupled from the magnetic nozzle throat.

All the measurements reported in this study are collected at an RF power of 250 W and an argon pressure of 0.5 mTorr ($\approx$ 70 mPa). Four different magnetic nozzle strengths are employed: (a) Case A, $B_{z,\mathrm{max}} = 77$ G, (b) Case B, $B_{z,\mathrm{max}} = 120$ G, (c) Case C, $B_{z,\mathrm{max}} = 175$ G, and (d) Case D, $B_{z,\mathrm{max}} = 330$ G, where $B_{z,\mathrm{max}}$ denotes the value of maximum magnetic field strength on axis. These values correspond to four different levels of ion magnetisation under the antenna: (a) $r_{\mathrm{L,i}} \geq R$, (b) $r_{\mathrm{L,i}} \sim R$, (c) $r_{\mathrm{L,i}} < R$, and (d) $r_{\mathrm{L,i}} \ll R$, where $r_{\mathrm{L,i}}$ is the ion Larmor radius on axis and R is the plasma source inner radius. Under these experimental conditions, the plasma density peaks axially in the source a few centimetres before the magnetic nozzle throat reaching a value of $n_{\mathrm{p}} \sim 10^{-17}$ m^{-3}, to then decrease to $n_{\mathrm{p}} \sim 10^{-16}$ m^{-3} during the expansion phase.

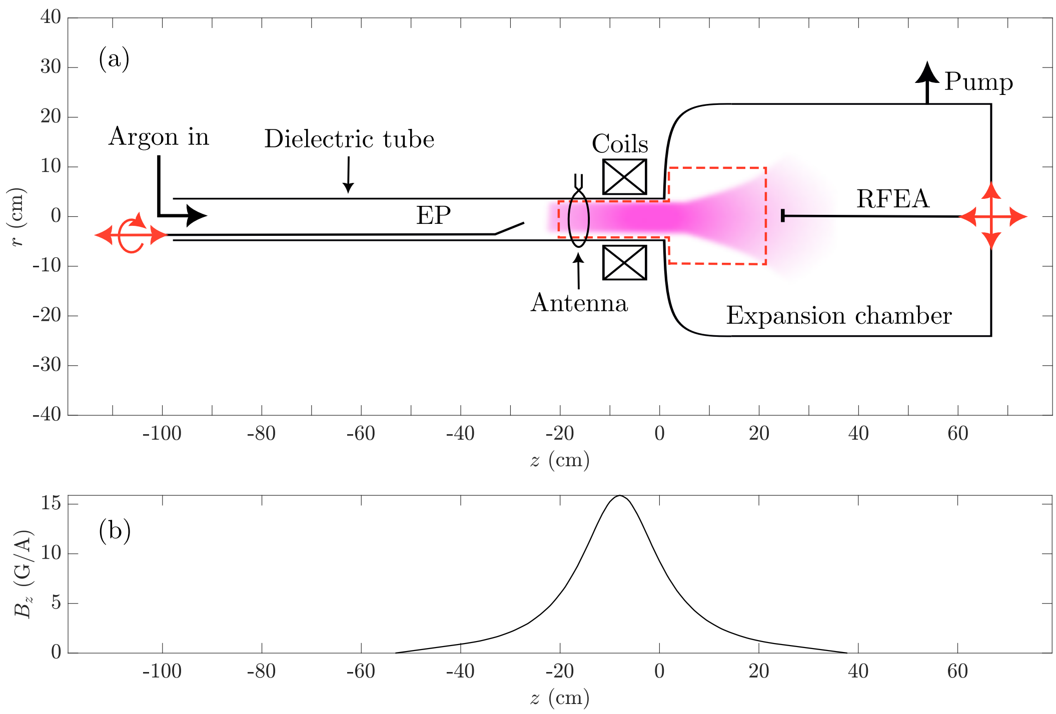

Figure 1: Schematic of the experimental set-up *Moa* (a), and plot of the magnetic field on axis (b). The red arrows indicate the directions in which the probes can move. The dashed red lines determine the boundary where measurements are conducted.

2.1 Diagnostics

A retarding field energy analyser (RFEA) is used to map the ion energy distribution function (IEDF), and the plasma V_{p} and ion beam V_{B} potentials in the expansion chamber. The design of the probe includes four mesh grids with a

DOI: 10.13009/EUCASS2023-282

transmission factor of 59% (i.e., earth, repeller, discriminator, and secondary grid), and a nickel collector plate. The repeller grid is biased to -90 V to ensure total electron rejection at the probe entrance. The discriminator grid is swept from 0 to +80 V to filter the ions according to their energy, and measure the *I*-*V* characteristics. The 2 mm diameter probe orifice is kept perpendicular to the incoming plasma flux to detect the presence of a directional ion beam. The RFEA is mounted on 1/4" stainless steel shaft, and custom-made vacuum feedthroughs allow the probe to move in the axial and radial direction. The IEDF is evaluated by differentiating the measured current I_C with respect to the discriminator voltage V_D through an analogue differentiator. The local plasma potential (corresponding to the zero-energy, background ion population) and ion beam potential (corresponding to the axially accelerated ion population) are then defined as the location of the first and second peaks on the energy distribution, respectively.[11–16] The design of the probe used in this study has been extensively used in similar experiments,[3,12,15,17] and a detailed description of the RFEA and the data processing can be found in Refs. [8,16].[8,16] The estimated error in the measured potentials is ±2 V.

As the size of the RFEA is comparable to the plasma source radius, the local plasma potential in the plasma source is measured using an emissive probe (EP) to minimise plasma disturbances. The probe is made with a U-shaped, 0.127 mm diameter tungsten wire inserted into a 2 mm outer diameter two-bore ceramic tube, and it is mounted on an axially movable 1/4" steel shaft covered by a dielectric tube. An isolated DC power supply is employed to heat up the tungsten filament to allow thermionic emission. The respective *I*-*V* characteristic is found by sweeping the current from 1.5 to 2.6 A in steps of 0.025 A. The plasma potential is then obtained by using the floating method,[18,19] and the estimated measurement error is ±2.75 V.

3. Results

3.1 Analysis of the Plasma Characteristics on Axis

As mentioned in Section 2.1, the retarding field energy analyser is used to map the plasma characteristics in the expansion chamber ($3 \le z \le 19$ cm), while the plasma potential in the source is measured using the emissive probe ($-23 \le z \le 3$ cm). Figure 2 shows the plasma V_p and ion beam V_B potential measured on axis for increasing magnetic field strength.

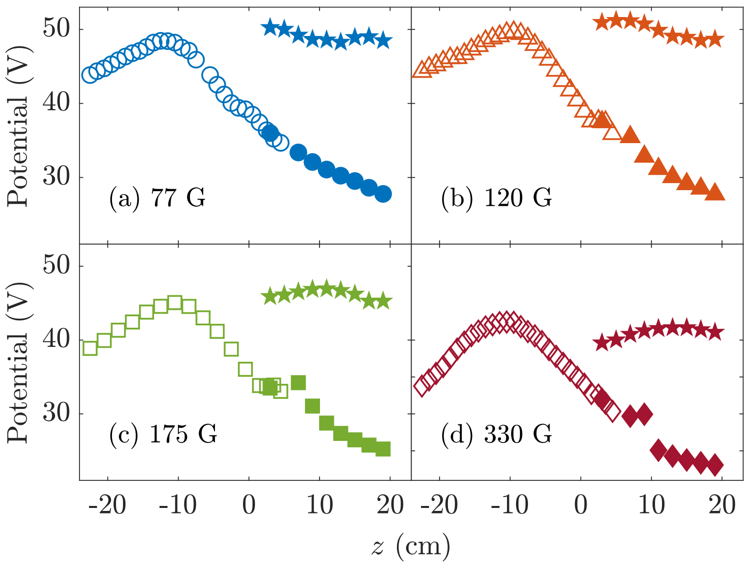

Figure 2: Plasma (various shapes) and ion beam potential (star-shaped markers) measured on axis for the different magnetic field cases. The filled markers correspond to the potentials measured with the RFEA.

The plasma potential on axis peaks in the source a few centimetres before the magnetic nozzle throat and then decreases rapidly. This monotonic decrease generates an ambipolar electric field that accelerates the ions created in the source as the plasma expands in the magnetic nozzle. In contrast, and as expected, the ion beam potential on axis stays roughly constant for all cases. It is interesting to note that an ion beam is detected by the RFEA even for the lowest magnetic field case. Table 1 summarises the maximum values of plasma potential measured by the emissive probe in the plasma source with the average ion beam potentials measured by the RFEA. As shown in table 1 and seen in fig. 2,

DOI: 10.13009/EUCASS2023-282

the value of V_B matches well the maximum value of plasma potential in the source. Thus, the supersonic ion population observed in *Moa* indeed corresponds to the plasma created in the source that gets accelerated by the potential drop.

While the value of the local plasma and beam potentials decreases with increasing $\vec{B}$ (e.g. $V_B \approx 50$ V for case B, while $V_B \approx 41$ V for case D), the magnitude of the potential drop on axis (≈ 0.5 V/cm) appears to not be significantly affected by the strength of the magnetic field. The V_p structure on axis in the plasma source agrees well with the Boltzmann relation $V_p(z) = V_p(z_0) + T_e \ln\left[n_p(z)/n_p(z_0)\right]$, assuming electron temperatures of $T_e = 5.5 - 6.5$ eV. These values compare well with measurements of T_e obtained with the RFEA in electron collection mode (not reported here as it is out of the scope of this study), thus validating the agreement with the Boltzmann relation.

Table 1: Comparison of maximum plasma potential $V_{p,max}$ measured in the source and the average ion beam potential $V_{B,avg}$ on axis, for each of the four values of $B_{z,max}$.

Case	$B_{z,max}$ (G)	$V_{\mathbf{p,max}}$ **(V)**	$V_{\mathbf{B,avg}}$ **(V)**
A	77	48	49
B	120	50	50
C	175	45	46
D	330	42	41

An indicator of the ion density near the probe entrance is provided by the total ion current. When the discriminator voltage is set to $V_D = 0$ V, all ions that can enter the RFEA sheath are collected. Figure 3(a) shows the total ion current $I_{0,tot}$ measured on axis with the RFEA. Similarly, the ion beam current I_B can be used to qualitatively assess the beam density. I_B can be obtained from the I-V curve characteristics and is defined as the current measured at the beam potential, i.e. $I_B = I_C(V_B)$.[20,21] It is important to note that the ion beam current I_B at potential V_B is a measurement of all the ions possessing an energy $\varepsilon_B \geq qV_B$. Hence, the other half of the ion beam population having an energy $\varepsilon_B < qV_B$ is not accounted for. For the purposes of this study, this definition of the ion beam current is deemed sufficient to qualitatively assess the properties of the accelerated ion population. Figure 3(b) shows I_B measured on axis for the magnetic field cases studied.

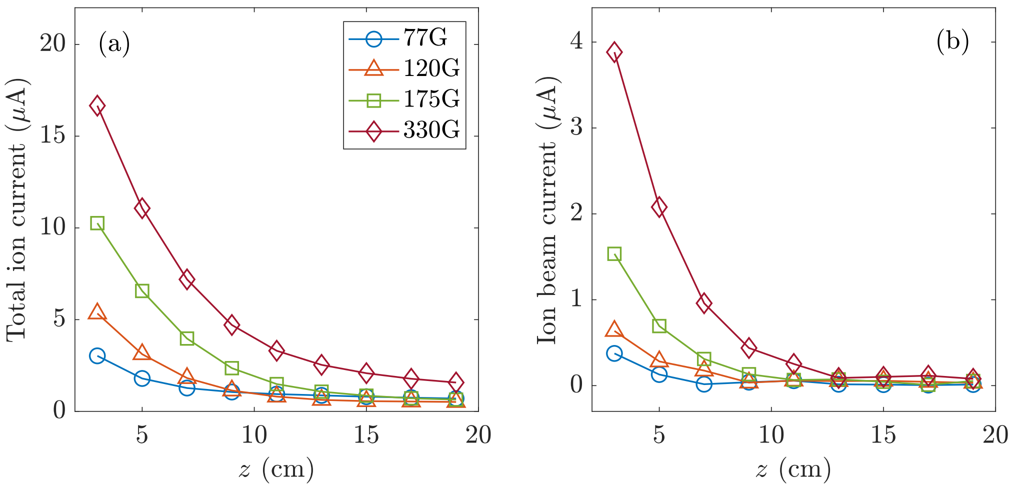

Figure 3: Total ion current (a), and ion beam current (b) measured with the RFEA on axis for the different magnetic field cases. The ion beam current was estimated from $I_B = I_C(V_B)$.

The profiles of both the total ion current and the ion beam current in fig. 3 show a similar behaviour. As expected, the value of the measured current increases for increasing magnetic field strength, and it decreases along the axis as a result of plasma expansion and ion-neutral charge-exchange collisions. The effects of the magnetic nozzle strength on the axial characteristics is evident when analysing the data collected for $B_{z,max} = 330$ G a few centimetres downstream from the plasma source exit. At $z = 3$ cm, the total ion current and the ion beam current are five and nine times higher than the currents measured at $B_{z,max} = 77$ G, respectively. Similarly, for the other cases studied, the growth rate of I_B with increasing field strength is observed to be greater than that of $I_{0,tot}$.

The radial profiles of the total ion current obtained from the I-V characteristics measured with the retarding field energy analyser are shown in figure 4. As it can be seen, the profiles exhibit an off-axis peak at at $r = \pm 5$ cm

DOI: 10.13009/EUCASS2023-282

for all magnetic field cases studied. These high-density conics have been associated with local ionisation occurring downstream from the magnetic nozzle, which could be caused by high energetic electrons travelling along the most peripheral magnetic field lines. The hollow structure has been observed both in numerical simulations and experimental studies in the diffusion region of an RF plasma expanding in a magnetic nozzle.[10, 22–30]

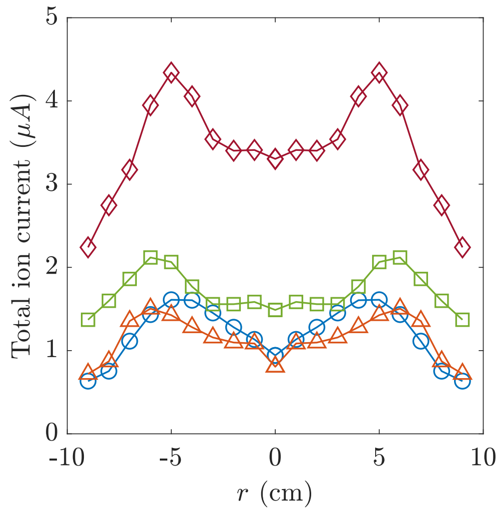

Figure 4: Total ion current measured radially by the RFEA in the expansion chamber at z = 11 cm for (a) $B_{z,\max}$ = 77 G (blue circles), (b) $B_{z,\max}$ = 120 G (orange triangles), (c) $B_{z,\max}$ = 175 G (green squares), and (d) $B_{z,\max}$ = 330 G (red diamonds). The data has been mirrored around r = 0 cm for clarity.

3.2 Ion Energy Distribution Functions in the Plasma Plume

Figure 5 shows an example of the *I*-*V* characteristics and ion energy distribution functions measured for increasing magnetic field strengths downstream the MN at $(r, z) = (0, 9)$ cm. As discussed in section 3.1, the values of the total ion and beam currents grow with increasing $\vec{B}$. This can also be seen in the *I*-*V* curves plotted fig. 5(a). Analysing the IEDFs on axis (fig. 5(b)), the ion beam population becomes more dominant with increasing magnetic field strength, correlating with the I_B data discussed in section 3.1. While at $B_{z,\max}$ = 77 G the thermal ions comprise the primary ion population and the ion beam peak is significantly lower, the population of the accelerated supersonic ions becomes predominant for the other $\vec{B}$ cases.

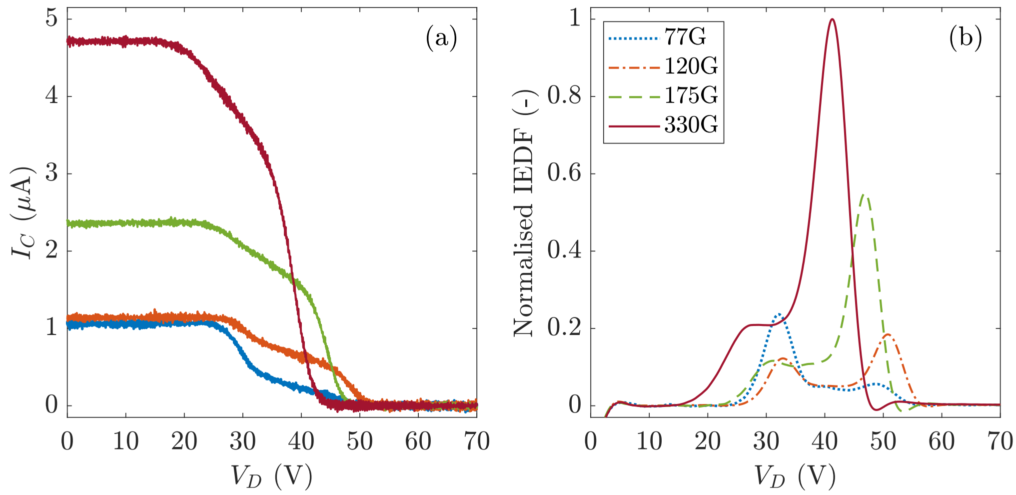

Figure 5: *I*-*V* characteristics (a), and ion energy distribution functions (b) measured for increasing magnetic field strengths at $(r, z) = (0, 9)$ cm. The energy distributions in (b) were normalised with the peak value measured for $B_{z,\max}$ = 330 G.

DOI: 10.13009/EUCASS2023-282

This behaviour is better seen in the contour plots shown in figure 6. The high energy peak corresponding to the ion beam population is clearly visible and dominates for the axial coordinates closer to the source exit. As the plasma expands, elastic and charge-exchange (CEX) collisions occur; thus, the density of the accelerated, high energy ion beam population reduces, while the number density of the background zero-energy ions is enhanced. The mean free path for ion-neutral collisions (CEX + elastic) in *Moa* for the operating pressure is $\lambda \sim 10$ cm, so the fast ions will collide with the neutrals as the RFEA covers the axial distance of the measurements. This is reflected by the increase in amplitude of the ion energy distribution around the plasma potential, and the corresponding decrease in the ion beam component for $z > 11$ cm.

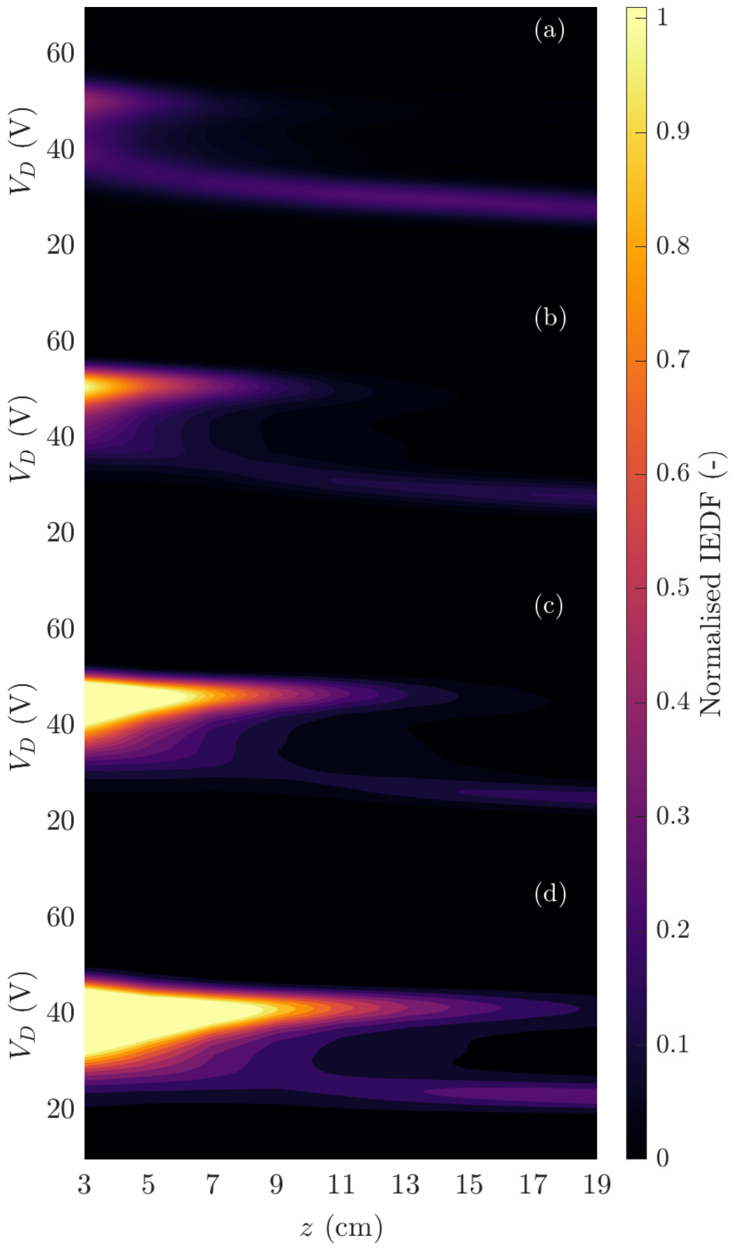

Figure 6: Contour plots of the ion energy distribution functions measured on axis for (a) $B_{z,\text{max}} = 77$ G, (b) $B_{z,\text{max}} = 120$ G, (c) $B_{z,\text{max}} = 175$ G, and (d) $B_{z,\text{max}} = 330$ G.

While the energy distribution of the background ion population does not change significantly with magnetic field strength, and peaks at $z > 13$ cm for all cases due to ion-neutral collisions, the structure of the supersonic ion beam is significantly affected by the magnitude of $\vec{B}$. The amplitude of the high energy ions distribution is more marked for higher magnetic field strengths, and peaks for $B_{z,\text{max}} = 330$ G (see fig. 6(d)). Additionally, the ion beam extends further downstream as $\vec{B}$ increases. The decrease in both plasma and beam potentials with increasing magnetic field

DOI: 10.13009/EUCASS2023-282

strength is also visible in fig. 6. Therefore, it is observed that the magnetic nozzle strength affects the axial transport and characteristics of the ion beam. This behaviour could be explained by the enhanced ion confinement as the magnetic field increases, which would contribute to a reduced cross-field diffusion.

3.3 Supersonic Ion Beam

The ion beam speed v_{beam} on axis can estimated from the following equation,

$$v_{\mathrm{beam}} = \sqrt{\frac{2\varepsilon_{\mathrm{B}}}{m_{\mathrm{i}}}}, \tag{1}$$

where $\varepsilon_{\mathrm{B}} = e(V_{\mathrm{B}} - V_{\mathrm{p}})$ is the energy of the beam. Thus, the larger the potential drop, the higher the ion beam speed.

Figure 7 shows the estimated v_{beam} on axis with increasing magnetic field. As shown in fig 2, the potential drop for the highest magnetic field case (330 G) is the smallest ($\varepsilon_{\mathrm{B}} \approx 18$ eV), resulting in the the lowest ion beam speed, which plateaus to a value of approximately 9 km/s for $z > 10$ cm. Conversely, for the magnetic field cases A, B and C, the potential drop is roughly invariant for increasing B_z ($\varepsilon_{\mathrm{B}} \approx 21$ eV), and the ion beam speed plateaus at ≈ 10 km/s. Given that the ion sound speed in the system is $c_{\mathrm{S}} \sim 4$ km/s, the maximum ion Mach number ($M = v_{\mathrm{beam}}/c_{\mathrm{S}}$) is estimated to range from $M = 2.2$ for $B_{z,\mathrm{max}} = 330$ G, to $M = 2.5$ for the lower magnetic nozzle configurations. As expected, the ion beam is accelerated to supersonic speeds by the ambipolar electric field. Similar ion beam speeds and plateau behaviour were observed in similar experiments.[5,12,27]

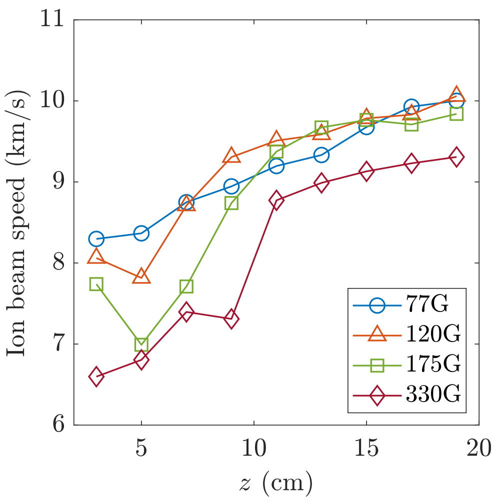

Figure 7: Ion beam speed on axis for the different magnetic field cases. The average error in v_{beam} is estimated to be ±780 m/s.

4. Conclusion

This study presents measurements of the axial evolution of a supersonic ion beam ($v_{\mathrm{beam}} \sim 9 - 10$ km/s) in a magnetic nozzle for increasing magnetic field strengths. The data was collected in a RF plasma device at The University of Auckland at an RF power of 250 W, and an argon pressure of 70 mPa. Four different magnetic field strengths were employed to conduct the experimental campaign, i.e. (a) case A, $B_{z,\mathrm{max}} = 77$ G, (b) case B, $B_{z,\mathrm{max}} = 120$ G, (c) case C, $B_{z,\mathrm{max}} = 175$ G, and (d) case D, $B_{z,\mathrm{max}} = 330$ G. Measurements of the ion and beam currents, plasma and ion beam potentials, ion beam speed, and ion energy distribution functions were obtained with a custom-build emissive probe and a four-grid retarding field energy analyser.

An ion beam was detected for all the magnetic configurations analysed. It was observed that the magnetic nozzle strength affected the ion beam characteristics in the plasma plume. While greater ion beam speeds were measured for the lower magnetic field strengths ($\approx 10\%$ increase), the ion beam current at the highest magnetic field strength (i.e., $B_{z,\mathrm{max}} = 330$ G) was found to be nine times higher than that for the lowest magnetic field case ($B_{z,\mathrm{max}} = 77$ G). This was reflected by the higher amplitude of the energetic ion distribution measured for higher magnetic field strengths.

DOI: 10.13009/EUCASS2023-282

Increasing magnetic field strength resulted in a decrease in both plasma and beam potentials, while the structure of the ambipolar electric field on axis remained approximately invariant. The axial transport of the ion beam was also observed to be modified by the magnetic nozzle strength. As the magnitude of $\vec{B}$ increased, the presence of an ion beam was detected over longer axial distances. This is thought to be the result of an enhanced plasma confinement at the strongest field configurations.

5. Acknowledgements

The research was mainly supported by the Asian Office of Aerospace Research and Development (AOARD), the international office of the Air Force Office of Scientific Research (AFOSR), under grant number #FA2386-19-1-4012.

References

[1] C Charles, P Alexander, C Costa, O Sutherland, R Boswell, L Pfitzner, R Franzen, J Kingwell, A Parfitt, P-E Frigot, J Gonzalez del Amo, and E Gengembre. Helicon Double Layer Thruster. *Collection of Technical Papers - AIAA/ASME/SAE/ASEE 42nd Joint Propulsion Conference*, 7, 07 2006.

[2] K Takahashi. Helicon-type radiofrequency plasma thrusters and magnetic plasma nozzles. *Reviews of Modern Plasma Physics*, 3:044510, 12 2019.

[3] W Cox, C Charles, R W Boswell, R Laine, and M Perren. Magnetic ion beam deflection in the helicon double-layer thruster. *Journal of Propulsion and Power*, 26(5):1045–1052, 2010.

[4] M Merino and E Ahedo. Contactless steering of a plasma jet with a 3D magnetic nozzle. *Plasma Sources Science and Technology*, 26:095001, 07 2017.

[5] R Imai and K Takahashi. Deflections of dynamic momentum flux and electron diamagnetic thrust in a magnetically steered rf plasma thruster. *Journal of Physics D: Applied Physics*, 55(13):135201, dec 2022.

[6] R Imai and K Takahashi. Demonstrating a magnetic steering of the thrust imparted by the magnetic nozzle radiofrequency plasma thruster. *Applied Physics Letters*, 118:264102, 06 2021.

[7] K Takahashi and R Imai. Two-dimensional deflection of a plasma plume exhausted from a magnetically steered radiofrequency plasma thruster. *Physics of Plasmas*, 29(5):054501, 2022.

[8] A Caldarelli, F Filleul, C Charles, R W Boswell, N Rattenbury, and J Cater. Radial characterization of an ion beam in a deflected magnetic nozzle. *Journal of Electric Propulsion*, 1(10):10, 2022.

[9] K Takahashi. Thirty percent conversion efficiency from radiofrequency power to thrust energy in a magnetic nozzle plasma thruster. *Scientific Reports*, 12:18618, 2022.

[10] K Takahashi, T Sugawara, and A Ando. Spatial measurement of axial and radial momentum fluxes of a plasma expanding in a magnetic nozzle. *New Journal of Physics*, 22(7):073034, 7 2020.

[11] C Charles. Hydrogen ion beam generated by a current-free double layer in a helicon plasma. *Applied Physics Letters*, 84(3):332–334, 2004.

[12] C Charles and R W Boswell. Laboratory evidence of a supersonic ion beam generated by a current-free “helicon" double-layer. *Physics of Plasmas*, 11(4):1706–1714, 2004.

[13] A M Keesee, E E Scime, C Charles, A Meige, and R Boswell. The ion velocity distribution function in a current-free double layer. *Physics of Plasmas*, 12(9):093502, 2005.

[14] Y Zhang, C Charles, and R Boswell. Effect of radial plasma transport at the magnetic throat on axial ion beam formation. *Physics of Plasmas*, 23(8):083515, 2016.

[15] A Bennet, C Charles, and R Boswell. In situ electrostatic characterisation of ion beams in the region of ion acceleration. *Physics of Plasmas*, 25(2):023516, 2018.

[16] A Caldarelli, F Filleul, R W Boswell, C Charles, N J Rattenbury, and J E Cater. Data processing techniques for ion and electron-energy distribution functions. *Physics of Plasmas*, 30(4):040501, 2023.

DOI: 10.13009/EUCASS2023-282

[17] C Bohm and J Perrin. Retarding-field analyzer for measurements of ion energy distributions and secondary electron emission coefficients in low–pressure radio frequency discharges. *Review of Scientific Instruments*, 64(1):31–44, 1993.

[18] J P Sheehan and N Hershkowitz. Emissive probes. *Plasma Sources Science and Technology*, 20(6):063001, 11 2011.

[19] J P Sheehan, Y Raitses, N Hershkowitz, and M McDonald. Recommended practice for use of emissive probes in electric propulsion testing. *Journal of Propulsion and Power*, 33(3):614–637, 2017.

[20] W Cox. *Magnetic steering of the ion beam in the helicon double layer thruster*. PhD thesis, Australian National University, 2010.

[21] T A Lafleur. *Helicon Wave Propagation in Low Diverging Magnetic Field*. PhD thesis, Australian National University, 2011.

[22] C Charles. High density conics in a magnetically expanding helicon plasma. *Applied Physics Letters*, 96(5):051502, 2010.

[23] N Gulbrandsen and Å Fredriksen. RFEA Measurements of High-Energy Electrons in a Helicon Plasma Device with Expanding Magnetic Field. *Frontiers in Physics*, 5, 2017.

[24] K Takahashi, H Akahoshi, C Charles, R W Boswell, and A Ando. High temperature electrons exhausted from rf plasma sources along a magnetic nozzle. *Physics of Plasmas*, 24(8):084503, 2017.

[25] S Ghosh, S Yadav, K K Barada, P K Chattopadhyay, J Ghosh, R Pal, and D Bora. Formation of annular plasma downstream by magnetic aperture in the helicon experimental device. *Physics of Plasmas*, 24(2):020703, 2017.

[26] A Bennet, C Charles, and R Boswell. Selective radial release of hot, magnetised electrons downstream of a low-pressure expanding plasma. *Journal of Physics D: Applied Physics*, 51(37):375204, 8 2018.

[27] A Bennet, C Charles, and R Boswell. Separating the location of geometric and magnetic expansions in low-pressure expanding plasmas. *Plasma Sources Science and Technology*, 27(7):075003, 7 2018.

[28] S Yadav, S Ghosh, S Bose, K Barada, R Pal, and P Chattopadhyay. Role of ion magnetization in formation of radial density profile in magnetically expanding plasma produced by helicon antenna. *Physics of Plasmas*, 25:043518, 04 2018.

[29] L Buschmann and Å Fredriksen. Axial and radial development of the hot electron distribution in a helicon plasma source, measured by a retarding field energy analyzer (rfea). *Plasma Sources Science and Technology*, 31(2):025005, 02 2022.

[30] K Emoto, K Takahashi, and Y Takao. Density profile transition and high-energy electron transport in a magnetically expanding radio frequency plasma. *Physics of Plasmas*, 30(1):013509, 2023.